ADVANCES IN ATMOSPHERIC SCIENCES, VOL. 30, NO. 3, 2013, 922–939

A Global Ocean Biogeochemistry General Circulation Model and its Simulations

XU Yongfu*[1] (徐永福), LI Yangchun[1] (李阳春), and CHU Min[2] (储 敏)

[1]*State Key Laboratory of Atmospheric Boundary Layer Physics and Atmospheric Chemistry, Institute of Atmospheric Physics, Chinese Academy of Sciences, Beijing* 100029

[2]*National Climate Center, Beijing* 100081

(Received 16 July 2012; revised 4 November 2012)

ABSTRACT

An ocean biogeochemistry model was developed and incorporated into a global ocean general circulation model (LICOM) to form an ocean biogeochemistry general circulation model (OBGCM). The model was used to study the natural carbon cycle and the uptake and storage of anthropogenic CO_2 in the ocean. A global export production of 12.5 Pg C yr^{-1} was obtained. The model estimated that in the pre-industrial era the global equatorial region within $\pm 15^{\circ}$ of the equator released 0.97 Pg C yr^{-1} to the atmosphere, which was balanced by the gain of CO_2 in other regions. The post-industrial air–sea CO_2 flux indicated the oceanic uptake of CO_2 emitted by human activities. An increase of 20–50 μmol kg^{-1} for surface dissolved inorganic carbon (DIC) concentrations in the 1990s relative to pre-industrial times was obtained in the simulation, which was consistent with data-based estimates. The model generated a total anthropogenic carbon inventory of 105 Pg C as of 1994, which was within the range of estimates by other researchers. Various transports of both natural and anthropogenic DIC as well as labile dissolved organic carbon (LDOC) were estimated from the simulation. It was realized that the Southern Ocean and the high-latitude region of the North Pacific are important export regions where accumulative air–sea CO_2 fluxes are larger than the DIC inventory, whereas the subtropical regions are acceptance regions. The interhemispheric transport of total natural carbon (DIC+LDOC) was found to be northward (0.11 Pg C yr^{-1}), which was just balanced by the gain of carbon from the atmosphere in the Southern Hemisphere.

Key words: ocean biogeochemistry model, natural carbon, anthropogenic carbon, meridional transport

Citation: Xu, Y. F., Y. C. Li, and M. Chu, 2013: A global ocean biogeochemistry general circulation model and its simulations. *Adv. Atmos. Sci.*, **30**(3), 922–939, doi: 10.1007/s00376-012-2162-0.

1. Introduction

Human activities have emitted a great amount of CO_2 into the atmosphere since pre-industrial times, about 45% of which has remained in the atmosphere and the rest has been stored in the ocean and the terrestrial ecosystem, leading to an increase in atmospheric CO_2 by over 100 ppmv. The oceans play an important role in the adjustment of the carbon cycle. Using observed ocean data of carbon-related variables, Sabine et al. (2004) estimated that the oceans have absorbed over 48%±9% of anthropogenic CO_2 from fossil fuel combustion and cement production. In order to accurately project the oceanic uptake of anthropogenic CO_2 under future global climate change, it is necessary to reduce the level of uncertainty in current estimates of the ocean carbon sink.

Over the last few decades, understanding the carbon cycle has greatly improved. In the reports of the Intergovernemental Panel of Climate Change (IPCC) (IPCC, 2001), progress on the carbon cycle has often been summarized, including a focus on the ocean carbon cycle. A core issue to be addressed for research on the ocean carbon cycle is how much carbon has been taken up and will be taken up in the ocean in the future. Generally, there are two categories for the estimation of storage and distributions of anthropogenic CO_2 in the ocean. The first category is es-

*Corresponding author: XU Yongfu, xyf@mail.iap.ac.cn

timation based on observations. Many estimates of air–sea CO_2 fluxes have been made according to the increased amount of observations. However, because of the difference among methods, the uncertainty of estimates varies considerably (IPCC, 2007). Those methods based on observations include estimates obtained from marine observations, atmospheric observations, and a combination of the two. Those estimations based on marine observations mainly involve the air–sea difference of partial pressure and observed dissolved inorganic carbon (DIC). The former is often called the ΔP_{CO_2} method, and the latter has been referred to as the ΔC^* method by Gruber et al. (1996), multiple linear regression analysis (Levine et al., 2008), and the inversion method. Using the ΔP_{CO_2} method and 3 million measurements of surface water P_{CO_2} Takahashi et al. (2009) obtained an air–sea CO_2 flux of 1.6±0.9 Pg C in the non-El Niño year of 2000. Using DIC and bomb ^{14}C data, as well as a suite of ocean general circulation models (OGCMs), in an inversion mode Sweeney et al. (2007) reported a CO_2 flux of 1.3±0.5 Pg C in 1995. However, Gruber et al. (2009) used Gloor et al.'s (2003) inversion method to estimate that the CO_2 flux was 1.7±0.4 Pg C yr^{-1} in 1995.

The second category for the estimation of oceanic uptake of CO_2 is model-based estimates. There is a greater than 50-year history for the development of ocean carbon cycle models, which are generally forward models. Such models are currently widely used, because they can compensate for the insufficient coverage of observations and can also be used for projecting future climate. The earliest model was the box model developed by Craig (1957), and a further well known box-diffusion model was later developed by Oeschger et al. (1975). Since then, many different modified box models and 2D models have been developed. With the development of the OGCM, the ocean carbon cycle model has also rapidly developed, including early models of the inorganic carbon cycle to models featuring biological processes. It should be pointed out that the perturbation model of anthropogenic CO_2 proposed by Sarmiento et al. (1992) is quite useful for direct comparisons of the uptake and storage of anthropogenic CO_2 between different OGCMs.

Carbon cycle models with biological processes can be divided into nutrient-restored models, where biological production in the euphotic zone is determined by relaxing model-predicted nutrients (phosphates) towards the observed nutrient distribution (e.g. Najjr et al., 1992, 2007; Marinov et al., 2008), and nutrient-based models, where biological production is a function of nutrient concentrations (e.g. Bacstow and Maier-Reimer, 1990; Mair-Reimer, 1993; Aumont et al., 1999), as well as models with an explicit ecosystem (e.g. Six and Mair-Reimer, 1996; Palmer and Totterdell, 2001; Aumont et al., 2003; Schmittner et al., 2005). These different types of models have been used to understand the processes of the carbon cycle. The Ocean Carbon Model Intercomparison Project (OCMIP) was launched 10 years ago. In the first phase, Orr et al. (2001) found that the simulated uptake of anthropogenic CO_2 from the four OGCMs studied agreed within ±19%. In the second phase, Doney et al. (2004) compared 13 OGCMs and found that a large difference of biogeochemical fields among the models was due to model physics. These comparisons demonstrate an important role of physical fields in the simulation of the carbon cycle.

The development of ocean carbon cycle models in China began relatively late. During the 1990s, different 1D, 2D and 3D models were established. The first inorganic ocean circulation carbon cycle model was put forwarded by Xing (1995). Then, Xing (2000) further investigated the role of biological processes in a global ocean carbon cycle model. Jin and Shi (1999) incorporated a biological process into the Geophysical Fluid Dynamics Laboratory Modular Ocean Model v2 to study the carbon cycle. The same authors also later estimated the uptake and storage of anthropogenic CO_2 in the global ocean (Jin and Shi, 2001). Their biological process was quite similar to that used in Bacastow and Maier-Reimer (1990). Researchers at the Institute of Atmospheric Physics (IAP) have been using OGCMs developed by the State Key Laboratory of Numerical Modeling for Atmospheric Sciences and Geophysical Fluid Dynamics (LASG/IAP) to study the ocean carbon cycle since the 1990s. Based on the physical fields from the first generation of the IAP's OGCM, Dong et al. (1994) and Pu and Wang (2000) developed a 2D carbon cycle model with biological processes to make offline simulations of the carbon cycle in the Atlantic and Indian Oceans, respectively. A global OGCM called L30T63 was examined by Li and Shi (2005) with carbon-14, and by Li et al. (2006, 2007) with trichlorofluoromethane (CFC-11). Xu and Li (2009) employed L30T63 to estimate the storage and distribution of anthropogenic carbon, and they ran two cases to state the global oceanic anthropogenic CO_2 uptake to be 1.64 and 1.73 Pg C yr^{-1} for the 1990s, and a global inventory of 86.4 and 92.7 Pg C of anthropogenic CO_2 at the end of 1994, which was smaller than the data-based estimate of 118±19 Pg C by Sabine et al. (2004). Using the LASG/IAP Climate system Ocean Model (LICOM), Li and Xu (2012) investigated the difference between the estimation of anthropogenic CO_2 in the Pacific Ocean based on the perturbation approach and the carbon cycle model with biological processes.

Although there are many different types of ocean carbon cycle models, all of them have different deficiencies for the simulation of some important characteristics of the ocean carbon cycle. Furthermore, large differences exist between the models. Thus, there is still debate on the exact figure of oceanic uptake of atmospheric CO_2. Improvement in the simulation of physical fields is a long-term target. As with OGCMs, ocean carbon cycle models require further modification. In addition, they represent an important component of earth system models that are currently being developed in different research institutions. It should be pointed out that our ocean biogeochemistry model has been coupled into the IAP climate model to study the interaction between the carbon cycle and climate change.

The purpose of this paper is to report on the development of a carbon biogeochemistry model developed by researchers at the IAP, and to incorporate the model into LICOM to study the natural carbon cycle in the global ocean and to estimate the uptake and storage of anthropogenic carbon. Here, natural carbon indicates carbon that is not affected by human activities, whereas anthropogenic carbon represents carbon emitted by human activities since pre-industrial times. For the model simulation, the results of natural carbon are defined as a steady state that is achieved under the forcing of a constant pre-industrial atmospheric CO_2 concentration.

2. Model and experiment description

2.1 *Ocean carbon biogeochemistry model*

The ocean carbon biogeochemistry model basically consists of two parts: the air–sea gas exchange and chemical thermodynamic processes at the surface, and the physical and biochemical processes in the interior ocean. The biochemical processes mainly consider the biological production process in the euphotic zone and the remineralization process below that, which includes five biologically utilized tracers of DIC, total alkalinity (TA), phosphate (PO_4^{3-}), labile dissolved organic carbon (LDOC) and dissolved oxygen (DO) (Fig. 1).

The air–sea CO_2 exchange is controlled by the difference in CO_2 partial pressure between the atmosphere and ocean. The atmosphere is treated as a well-mixed box. Thus, the exchange flux of $CO_2(F)$ can be written as

$$F = k_{CO_2}\alpha\,(P_{CO_{2a}} - P_{CO_{2o}})\,(1-\gamma_{ice})\ , \qquad (1)$$

where k_{CO_2} is the transfer velocity of CO_2 from Wanninkhof's (1992) formula that is a function of wind speed and seawater temperature, γ_{ice} is the fraction of

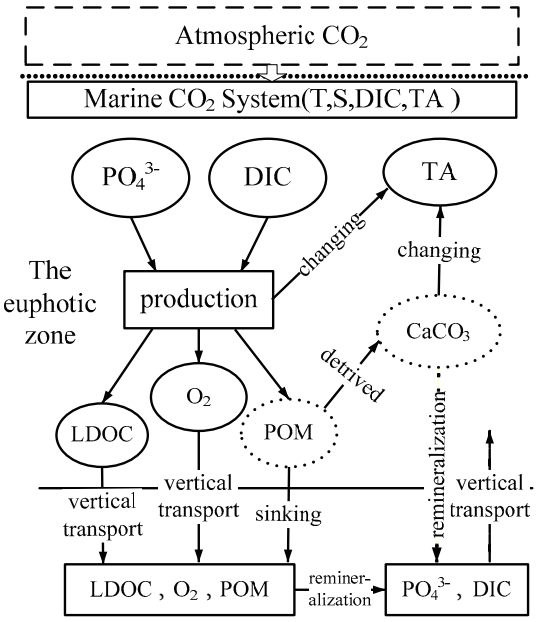

Fig. 1. Schematic diagram of the ocean carbon biogeochemistry model. The variables in the solid circles indicate prognostic ones, whereas the variables in the dashed circles indicate intermediate ones.

sea ice cover, α is the solubility of CO_2 from Weiss (1974), and $P_{CO_{2a}}$ and $P_{CO_{2o}}$ indicate the partial pressure of CO_2 in the atmosphere and ocean, respectively. The $P_{CO_{2o}}$ is a function of temperature, salinity, TA and DIC. Under the given condition, it can be computed with the iteration method through full chemical thermodynamic equations of the CO_2 system (Xu, 1992).

Similar to the air–sea CO_2 exchange, oxygen in the ocean exchanges with the atmosphere, and its air–sea flux (F_{O_2}) can be expressed as

$$F_{O_2} = k_{O_2}([O_{2sat}] - [O_{2o}])(1-\gamma_{ice})\ , \qquad (2)$$

where k_{O_2} is the transfer velocity of oxygen, and its calculation method is the same as that used for CO_2. $[O_{2sat}]$ and $[O_{2o}]$ indicate the equilibrium concentration of oxygen in air with water saturation under local atmospheric pressure and the simulated surface water dissolved oxygen concentration, respectively. $[O_{2sat}]$ can be further expressed as $[O_{2sat}] = [O_{2sato}] \cdot P/P_0$, where $[O_{2sato}]$ is the saturation concentration under standard conditions, P is local pressure, and P_0 is 1 atm. $[O_{2sato}]$ can be calculated from simulated temperature and salinity using the formula by Garcia and Gordon (1992).

After CO_2 enters into the surface layer, the marine CO_2 system can quickly reach a new equilibrium. Then, DIC is transported into the deep water, which is governed by circulation fields and biochemical pro-

cesses to obtain a redistribution. As with other prognostic variables of the carbon cycle model, the governing equation for DIC can be written as

$$\frac{\partial C}{\partial t} + \boldsymbol{v} \cdot \nabla C = \nabla_{\mathrm{h}} \cdot (K_{\mathrm{h}} \nabla_{\mathrm{h}} C) + \frac{\partial}{\partial z}\left(K_{\mathrm{v}} \frac{\partial C}{\partial z}\right) + \phi\,(C)\ , \qquad (3)$$

where C is DIC concentrations in the ocean, $\boldsymbol{v}$ is Euler velocity plus eddy-induced transport velocity, K_{h} represents diffusion coefficients, K_{v} is vertical diffusivity, and ϕ(C) represents biological sources and sinks.

The biological source and sink for DIC can be divided into two parts: the conversion of inorganic matter into organic matter through the photosynthetic processes in the euphotic zone, and the remineralization of organic matter below the euphotic zone. In this work, we considered that the biological process is driven by phosphate (e.g. Bacastow and Maier-Reimer, 1990; Maier-Reimer, 1993; Aumont et al., 1999). Organic matter indicates particulate and dissolved organic matter (POM, DOM). According to the third generation of Hamburg model of ocean carbon cycle (HAMOCC3) approach for the calculation of production in the euphotic zone (Maier-Reimer, 1993), the production (A_1) in the euphotic zone in our model is calculated as

$$A_1 = L_{\mathrm{f}} \times r_0 \times \left[\mathrm{PO}_4^{3-}\right] \frac{\left[\mathrm{PO}_4^{3-}\right]}{\left(h_{\mathrm{f}} + \left[\mathrm{PO}_4^{3-}\right]\right)} \times e^{-kz} \times \frac{T + 2.0}{T + 10.0}\ , \qquad (4)$$

where $[\mathrm{PO}_4^{3-}]$ is the simulated phosphate concentration in units of μmol kg^{-1}; L_{f} is the normalized solar factor; r_0 is the production rate, taken as 0.5 per month; h_{f} is the half saturation constant of phosphate, taken as 0.02 μmol L^{-1} (Eppley et al., 1969; Maier-Reimer, 1993); k is a decay constant; z is the central depth of each cell in the euphotic zone; and T is temperature. Although there are several different forms of dissolved organic carbon in the ocean, only LDOC is simulated in our model. As a result, A_1 can be divided into two parts: particulate organic phosphorus (POP) and labile dissolved organic phosphorus (LDOP). An equal fraction was used in this work. On this basis, the variables relating to carbon and their biological sources and sinks can be derived from the production and the stoichemical ratios (C:N:P =120:16:1) of carbon, nitrogen and phosphorus, directly and indirectly. In the same way, POP and LDOP are converted to POC and LDOC. The other ϕ terms are described in the following subsections.

2.1.1 *Phosphate*

The biological source and sink for phosphate is written as

$$\phi(\mathrm{PO}_4^{3-}) = -A_0 - \frac{B_0}{r_{\mathrm{cp}}}\ . \qquad (5)$$

It can be seen from Eq. (5) that the source and sink for phosphate consists of two parts. The first term (A_0) on the right hand side of Eq. (5) represents the production and remineralization of POP. The second term (B_0/r_{cp}) represents the production and remineralization of LDOP, where in fact B_0 is the production and remineralization of LDOC. r_{cp} in Eq. (5) is the ratio of C to P, taken as 120:1. The production and remineralization of POP (A_0) can be expressed as

$$A_0 = (1 - \delta_z)\,(1 - \sigma)\,A_1 - \delta_z \frac{\partial A_2}{\partial z}\ , \qquad (6)$$

$$A_2 = (1 - \sigma) \int_0^{z_{\mathrm{e}}} A_1 dz \times \left(\frac{z}{z_{\mathrm{e}}}\right)^{-0.858}\ , \qquad (7)$$

where σ is set to 0.5, and δ_z is set to 0 in the euphotic zone and 1 below that. A_2 in Eq. (6) is the vertical flux of POP below the euphotic zone. z_{e} in Eq. (7) is the thickness of the euphotic zone, taken as 100 m in our model. Because the export production is only considered in the model, the remineralization process takes place immediately below the euphotic zone. It is assumed that remineralization is completed momentarily. The term B_0 is described in LDOC cycling.

2.1.2 *LDOC*

The source and sink for LDOC can be described as:

$$\phi\,(\mathrm{LDOC}) = B_0 = B_1 - B_2\ , \qquad (8)$$

where B_1 is the production of LDOC in the euphotic zone, and B_2 is the remineralization below that, which can be further expressed as

$$B_1 = r_{\mathrm{cp}} \sigma\,(1 - \delta_z)\,A_1\ , \qquad (9)$$

$$B_2 = k_z \delta_{\mathrm{d}}\,[\mathrm{LDOC}]\ . \qquad (10)$$

Remineralization of LDOC only occurs in the region where LDOC is larger than 0. This means that when [LDOC]>0, δ_{d} is set to 1, whereas when [LDOC]$\leqslant$0, δ_{d} is 0. It is generally considered that remineralization occurs as a first-order decay process at all depths, and the decay constant k_z is a function of depth (Anderson and Sarmiento, 1995):

$$k_z = k' e^{\frac{z_{\mathrm{e}} - z}{750}}\ . \qquad (11)$$

The constant k' is set at each time step to conserve total LDOC globally, indicating that the remineralized LDOC below the euphotic zone is equal to the production of LDOC in the euphotic zone.

2.1.3 *TA*

The source and sink for TA depends on the consumption and reproduction of nutrients (phosphate), as well as the change in calcium carbonate, which can be expressed as

$$\phi\,(\mathrm{TA}) = r_{\mathrm{np}}\left(A_0 + \frac{B_0}{r_{\mathrm{np}}}\right) - 2C_{\mathrm{ca}}\,, \qquad (12)$$

where C_{ca} is the production of biogenic calcium carbonate that is related to the production of POC in the euphotic zone and the dissolution below that. The value of 0.07 for the rain ratio recommended by Yamanaka and Tajika (1996) is used in our model. r_{np} is the ratio of N to P, taken as 16:1.

2.1.4 *DIC*

The source and sink for DIC consists of three parts, including the production and remineralization of POC and LDOC, as well as the production and dissolution of calcium carbonate, which can be expressed as

$$\phi\,(\mathrm{DIC}) = -r_{\mathrm{cp}}A_0 - B_0 - C_{\mathrm{ca}}\,. \qquad (13)$$

2.1.5 *DO*

The source and sink for DO can be determined by the ratio of phosphate to DO through the production process. Yamanaka and Tajika (1996) considered that in the absence of oxygen, the dissolution of organic matter is not due to the oxidation reaction but to denitrification. Therefore, remineralization can always occur regardless of oxygen concentration. OCMIP-2 (Najjar et al., 2007) also employed this treatment of DO, and assumed that when DO is smaller than the given level of $[\mathrm{O_2}]^0$, the consumption of DO stops but remineralization of organic matter is still going on. $[\mathrm{O_2}]^0$ is taken as 4 μmol kg^{-1}. Our model employs this treatment, that is

$$\phi(\mathrm{O_2}) = \begin{cases} r_{\mathrm{o2P}}\phi(\mathrm{PO_4^{3-}}) & [\mathrm{O_2}] > [\mathrm{O_2}]^0 \\ 0 & [\mathrm{O_2}] \leqslant [\mathrm{O_2}]^0 \end{cases}\,, \qquad (14)$$

where $\phi(\mathrm{PO_4^{3-}})$ is the source and sink for phosphate, and r_{o2P} is the molar ratio of DO to phosphate, taken as −170 (Najjar et al., 2007).

2.2 *OGCM*

In order to run the biogeochemistry model and to study the storage, transport and distribution of natural and anthropogenic carbon in the ocean, an OGCM was required. Here, an OGCM called LICOM developed by the LASG/IAP, Chinese Academy of Sciences, was employed. A detailed description of the first version of LICOM, with a horizontal resolution of 0.5°×0.5° and a quasi-global domain (the Arctic Ocean is excluded) can be found in Liu et al. (2004). With the same framework, the model used in this work was a global ocean model from 78°S to 90°N, with a horizontal resolution of 2°×2°. LICOM has also been used to study the carbon cycle (Li and Xu, 2012; Li et al., 2012). Therefore, here we describe the LICOM model only in brief.

LICOM is made up of a primitive equation, free surface ocean general circulation model, with η-vertical coordinates and the Arakawa B-grid scheme in the absence of sea ice. Some parameterization schemes are employed in the model, including the penetration of solar radiation, a Richardson-number-dependent vertical mixing process in the tropical ocean, an isopycnal mixing scheme of tracers with an eddy-induced transport velocity according to Gent and McWilliams (1990) and Gent et al. (1995). Both isopycnal and thickness (skew) diffusivities of the isopycanal mixing scheme are taken to be 1.0×10^3 m^2 s^{-1}. For the vertical diffusion coefficient, it is taken to be a constant of 0.3×10^{-4} m^2 s^{-1} in the extratropical region. The vertical direction has 30 levels, with 15 levels in the upper 150 m of equal spacing and another 15 levels that are unequally spaced. The top level is 10 m thick, and the maximum depth is 5600 m.

The OGCM was driven at the surface by climatological monthly mean boundary conditions of thermal fluxes, salinity and wind stress. SST and sea surface salinity (SSS) were from the World Ocean Atlas 1998 (WOA98) (http://www.nodc.noaa.gov/), and other forcing data were from the Max-Planck-Institute–Ocean Model Intercomparison Project (MPI-OMIP) climatological monthly mean data (Roeske, 2001). The fluxes of salinity were calculated by the restoring method with a time scale of 10 days. A simple Newton cooling condition was used for the thermal flux. Because of the absence of the sea ice model, to produce realistic physical fields of circulation and water mass distributions, the restoration method of temperature at the surface layer was introduced into the model with a time scale of six days for the sea ice area.

2.3 *Numerical experiments*

It is generally considered that, until the Industrial Revolution, the CO_2 exchange between the atmosphere and ocean reached a steady state because of long-term interaction. This means that the global total air–sea CO_2 flux was close to 0 in the pre-industrial era. At that time the carbon present in the ocean is referred to as natural carbon.

After the OGCM was integrated for 1000 years under the climatologcial seasonally varying forcing, we coupled the carbon biogeochemistry model into the OGCM to form an ocean biogeochemistry gen-

eral circulation model (IAP-OBGCM), and spun up the OBGCM from the physical field at the end of the first integration phase of the OGCM and from the observed profiles of DIC, TA, and phosphate from WOA05 and the Carbon Dioxide Information Analysis Center (CDIAC) (http://cdiac.ornl.gov). The initial concentrations of LDOC and dissolved oxygen were 4.2 μmol kg^{-1} and 170 μmol kg^{-1}, respectively. In this work, climatological wind speed was used, and the data were from Esbensen and Kushnir (1981). In order to take the change in surface salinity into account, a restoration term of TA was included in the model with a time scale of 10 days. The statistical relationship between TA and salinity by Millero et al. (1998) was used.

The carbon cycle model was integrated for over 4000 years under the forcing of fixed atmospheric CO_2 at 278 ppmv, which was defined here as the pre-industrial value in 1800. As a result, the global total air–sea CO_2 flux was small enough to be ignored (smaller than 0.01 Pg C yr^{-1}), which was called the steady state pre-industrial results. On the basis of the pre-industrial results, the OBGCM was further integrated for 209 years from 1800 to 2008 under the prescribed atmospheric CO_2 concentration from Enting et al. (1994) and CDIAC (http://cdiac.ornl.gov).

3. Results and discussion

3.1 *Surface distribution characteristics of the pre-industrial variables*

Figure 2 shows both the observed and simulated surface distributions of phosphate concentrations. The observations are from WOA05 (Garcia et al., 2006b), and the simulated results are annual mean values at the end of 4200 years of integration. The observations reveal an obvious meridional gradient.

Since phosphate concentrations increase with depth in the upper ocean, high surface phosphate concentrations are mainly caused by vertical movement. Except that in the equatorial Pacific and the region around the Antarctic, upwelling induces high surface phosphate concentrations; the regions with a large surface mixed layer depth (Fig. 3) generally have large surface phosphate concentrations. However, in the Northwest Atlantic where there is strong vertical mixing and meanwhile biological consumption of phosphate is large (Wu et al., 2000); the simulated and observed phosphate is lower than that in other regions with strong vertical mixing. Because our simulated surface mixed layer depth is in good agreement with the data-based estimate, distributions of high surface phosphate concentrations are also consistent with those of the observations. The main difference between the simulation and observations is in the Northwest Pacific, particularly in the region around (50°N, 170°W) (near Kumchatka), where the simulated largest value is 1.2 μmol kg^{-1} lower than the observed one. Nevertheless, our results are in agreement with those of the third (Maier-Reimer, 1993) and fifth (Aumont et al., 2003) generation of HAMOCC.

Figure 4 shows the distribution of global annual mean export production from the model. In the region with high phosphate, export production is also relatively high. However, because of impacts of temperature and irradiation, in the high-latitude region, the latitude with high export production is lower, relative to the latitude with high phosphate. As a result, three main high regions are formed, including the regions of 30°–60°N and 30°–60°S, as well as the eastern equatorial Pacific. Meanwhile, in the coastal upwelling regions, export production is also very high. These results are close to those from the Sea-viewing Wide Field-of-view Sensor (SeaWiFS) ocean color data and those by Laws et al. (2000) who used the f-ratio method proposed by Eppley and Peterson (1979). The f-ratio is the ratio of new production to total production. However, compared to the results of Laws et al. (2000) who considered the influences of temperature and net photosynthetic effect on the f-ratio, our simulated results are higher in the equatorial region and the Southern Ocean, and lower in the subpolar region

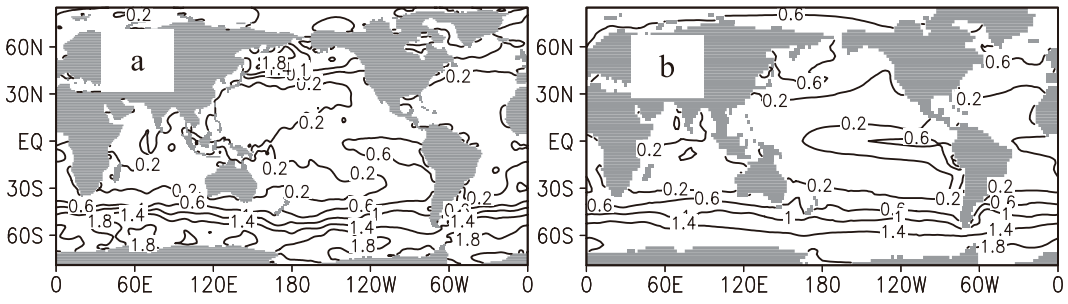

Fig. 2. Surface distribution of annul mean phosphate concentration (μmol kg^{-1}): (a) observation and (b) simulation. Contour intervals are 0.4 μmol kg^{-1}.

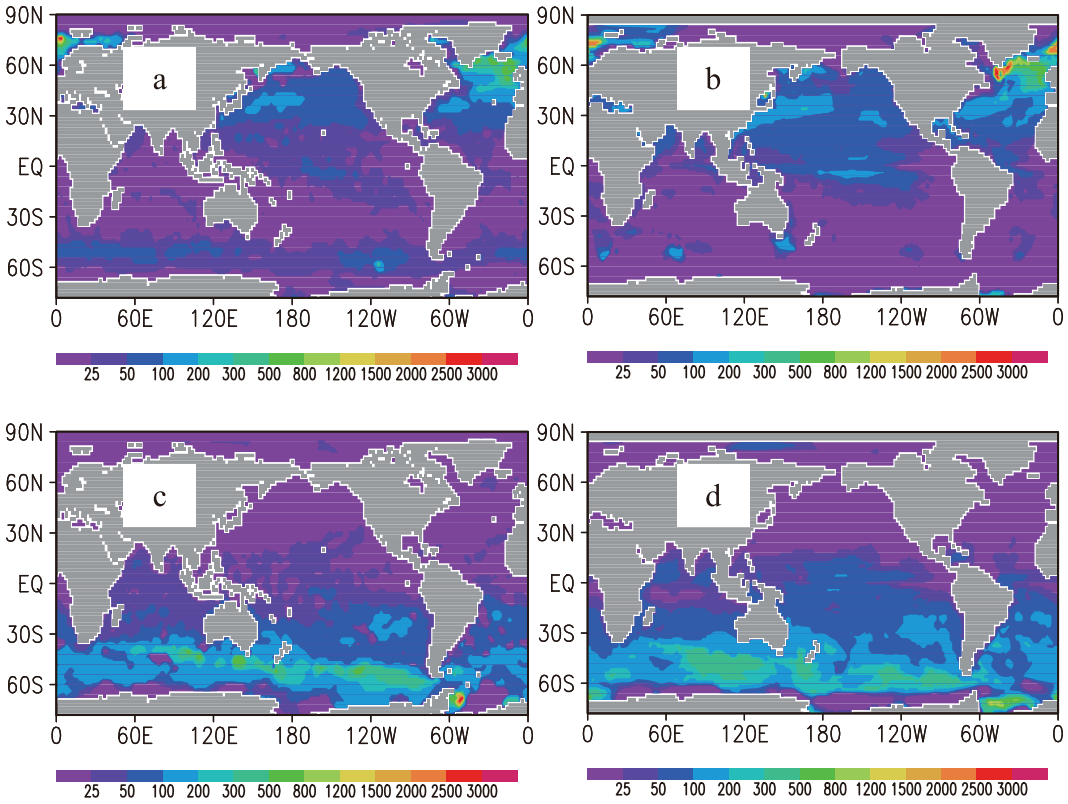

Fig. 3. (a, b) January and (c, d) July mixed-layer depth (m) in (a, c) WOA05 and (b, d) model, based on a $\Delta\sigma_\theta$ =0.1 kg m^{-3}.

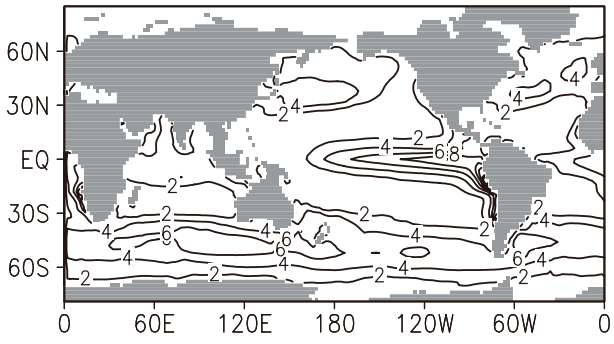

Fig. 4. Distribution of annual export production (mol m^{-2} yr^{-1}).

of the North Pacific and the region north of 30°N in the North Atlantic. Our model gives rise to annual export production of 12.5 Pg C yr^{-1}, which is larger than the 11.1 Pg C yr^{-1} of Laws et al. (2000) and the inversion result of 9.8 Pg C yr^{-1} reported by Schlitzer (2002), but smaller than the average value of 17±6 Pg C yr^{-1} from the 11 OCMIP-2 models (Phase II of the Ocean Carbon Model Intercomparison Project) (Najjar et al., 2007).

Because of impacts of oxygen solubility, distributions of surface dissolved oxygen reveal an obvious meridional gradient (Fig. 5). WOA05 observations (Garcia et al., 2006a) show a minimum DO of below 200 μmol kg^{-1} in the tropical regions, and a maximum DO of over 340 μmol kg^{-1} in the subpolar regions of both hemispheres. Our model reproduces well this observed feature, and in most regions the simulated values are also close to the observed ones. The main difference between observations and simulations appears to be in tropical regions and high-latitude regions of the North Pacific, where the simulated results are higher than the observed ones. In the eastern equatorial Pacific, the cold tongue is overestimated in our model, relative to the observations (about 1°C lower than the WOA05 value), leading to more oxygen dissolved in this region.

Unlike dissolved oxygen, which is strongly affected by temperature, distribution characteristics of surface TA are very similar to those of salinity, which are consistent with those of fresh water fluxes. As shown in Fig. 6, the observed surface TA (Key et al., 2004) is high in the subtropical regions where evaporation is high, and is low in the tropical regions where precipitation is high. In the high-latitude regions, formation of biogenic calcium carbonate further reduces surface TA (IPCC, 2007). Our model considers the impacts of

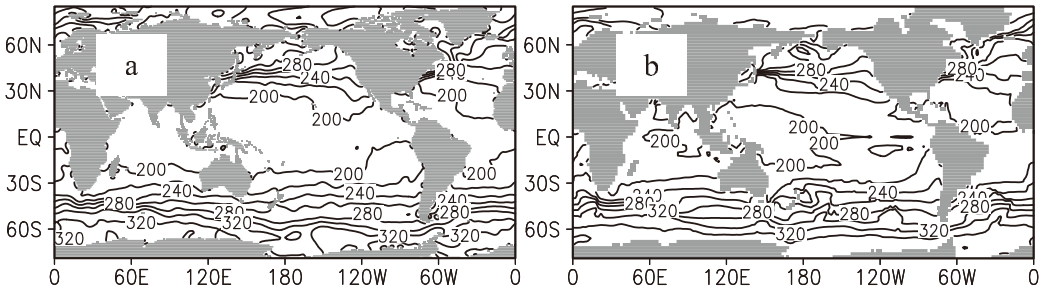

Fig. 5. The same as Fig. 2 but for DO. Contour intervals are 20 μmol kg^{-1}.

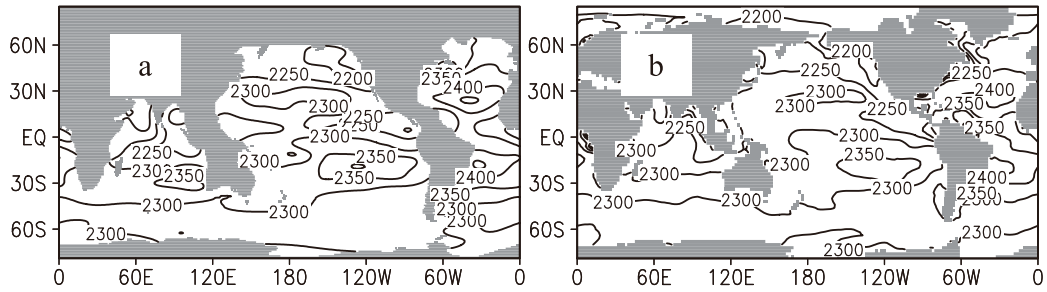

Fig. 6. The same as Fig. 2 but for TA. Contour intervals are 50 μmol kg^{-1}.

these factors on surface TA. TA restoration in surface water is conducted through the statistical relationship between TA and salinity (Millero et al., 1998). The influence of the formation of biological calcium carbonate on the change in TA is also included in the model (Eq. 12). The simulated results are in good agreement with observations. The main difference appears to be in the subtropical regions, particularly in the subtropical region of the North Atlantic, because simulated salinity is relatively smaller (not shown), leading to TA being underestimated by 20 μmol kg^{-1}.

Figure 7 shows the distribution of annual mean surface DIC concentrations from both observations and the simulation. Because the observations are from the Global Ocean Data Analysis Project (GLODAP) dataset, which was mainly obtained in the period 1989–95 (Key et al., 2004), the observed values should be larger than the pre-industrial surface water values, which means that our simulated results should be smaller than the observations. It has been recognized that anthropogenic carbon is about a few tens of micromoles per kilogram of sea surface water, as shown in Sabine et al. (2004), which should be the difference between present-day and natural DIC.

As with the observations, the simulated DIC shows a sharp polarward increase. In the same latitude band, the area with low temperatures has the relatively higher DIC, which indicates the importance of CO_2 solubility for the distribution characteristics of DIC. On the regional distribution characteristics, we see that in the Antarctic circumpolar region DIC is zonally relatively homogeneous. Surface DIC concentrations in the Atlantic Ocean are generally higher than those in the Pacific Ocean. Except that in the

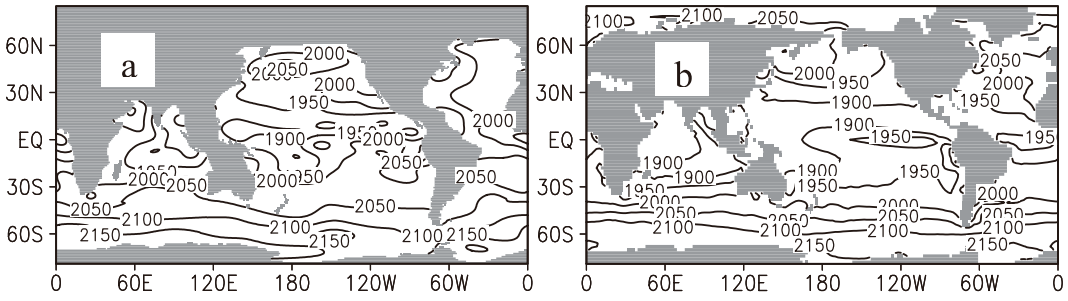

Fig. 7. The same as Fig. 2 but for DIC. Contour intervals are 50 μmol kg^{-1}.

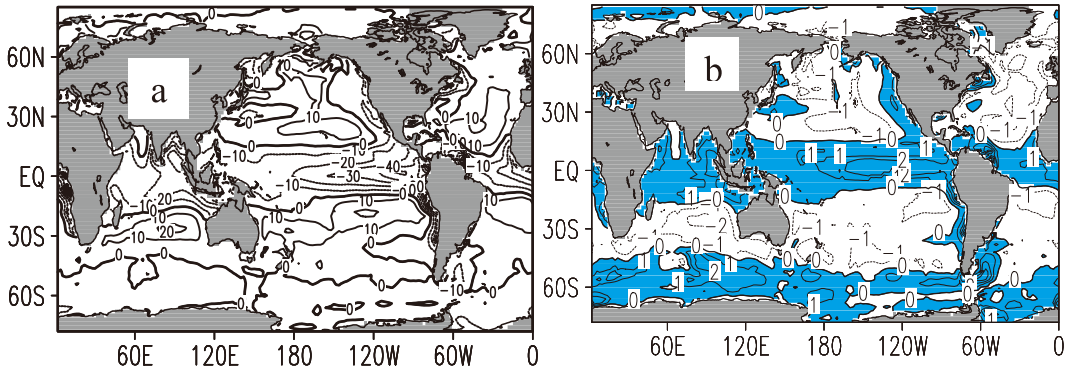

Fig. 8. Distributions of (a) pre-industrial air–sea P_{CO_2} difference ($P_{CO_{2a}} - P_{CO_{2o}}$, μatm) and (b) annual air–sea CO_2 fluxes (mol m^{-2} yr^{-1}).

equatorial Pacific where there is a strong upwelling, DIC concentrations in the tropical region are east-high and west-low, and in the Atlantic and Indian oceans tropical DIC concentrations are basically east-low and west-high. These are in good agreement with the observations, indicating that our model has a good description of physical and biochemical processes in the upper ocean. Compared to the simulated natural DIC results obtained by Maier-Reimer (1993), Jin and Shi (1999) and Xing (2000), which are even higher than the observed results obtained in the 1990s in many regions, our results are more reasonable.

Under combined effects of these variables, the distribution of the air–sea P_{CO_2} difference and CO_2 fluxes in the pre-industrial era displays the CO_2 loss in the tropical regions and the region south of 45°S, and the CO_2 gain in the subtropical regions (Fig. 8). High emissions appear to be in regions such as the eastern equatorial Pacific, with strong upwelling, and in the convection region of the Southern Ocean. The smallest −40 μatm contour appears to be near the eastern equatorial Pacific (0°, 100°W). In these regions, the supplement of DIC-rich deep water and relatively low surface TA generate high $P_{CO_{2o}}$, leading to high emissions. However, in the subtropical regions, high TA generates $P_{CO_{2o}}$ lower than $P_{CO_{2a}}$, leading to uptake. These distribution characteristics in the Southern Hemisphere are strongly consistent with those reported by Gruber et al. (2009) who employed an inversion model. In the region north of 20°N, most regions are sinks of natural carbon, in which the region of North Atlantic Deep Water (NADP) formation is a main uptake region of natural carbon, because of low sea surface temperature and vertical transport processes of carbon during the formation of NADP. This result is in agreement with that obtained from the inversion method by Mikaloff Fletcher et al. (2007). Accumulative calculation shows that the equatorial region (within ±15° of the equator) releases 0.97 Pg C yr^{-1} to the atmosphere, which is balanced by the uptake of 0.54 and 0.43 Pg C yr^{-1} in the Northern (north of 15°N) and Southern (south of 15°S) Hemisphere, respectively. This is in good agreement with the results of Murnane et al. (1999), although our values are 10%–28% smaller.

3.2 *Distributions of total carbon and anthropogenic carbon in the 1990s*

Anthropogenic carbon is generally considered to be carbon emitted by human activities. Anthropogenic carbon in the ocean can be defined as excess carbon relative to natural carbon in the pre-industrial era. For the comparison, observations in the 1990s are again shown in Fig. 9a (same as Fig. 7a). The simulated 10-yr average total DIC (natural+anthropogenic carbon) concentration in the 1990s is shown in Fig. 9b. Compared with natural carbon in the pre-industrial age (Fig. 7b), after about 200 years the DIC values have increased obviously, although the distribution characteristics of surface DIC are almost unchanged. The increment in most regions exceeds 40 μmol kg^{-1}. The simulated results are in good agreement with the observations (Fig. 9a), except in high-latitude regions of the North Atlantic. The model overestimates the observations by over 20 μmol kg^{-1} in the region north of 55°N in the North Atlantic. This is probably due to low production in this region, and also related to weak formation of North Atlantic Deep Water (NADW) from the model.

Figures 9c and d show the difference between the DIC average for the 1990s and the natural DIC level in pre-industrial times, i.e. excess carbon (anthropogenic carbon). The data-based estimate is from GLODAP (Key et al., 2004). Unlike Figs. 9a and b, the data in Figs. 9c and d are from a depth of 75 m. As mentioned in Li and Xu (2012), there are some obvious differences between the simulated results and data-based estimates in surface water. The data for anthropogenic carbon cannot be obtained from direct

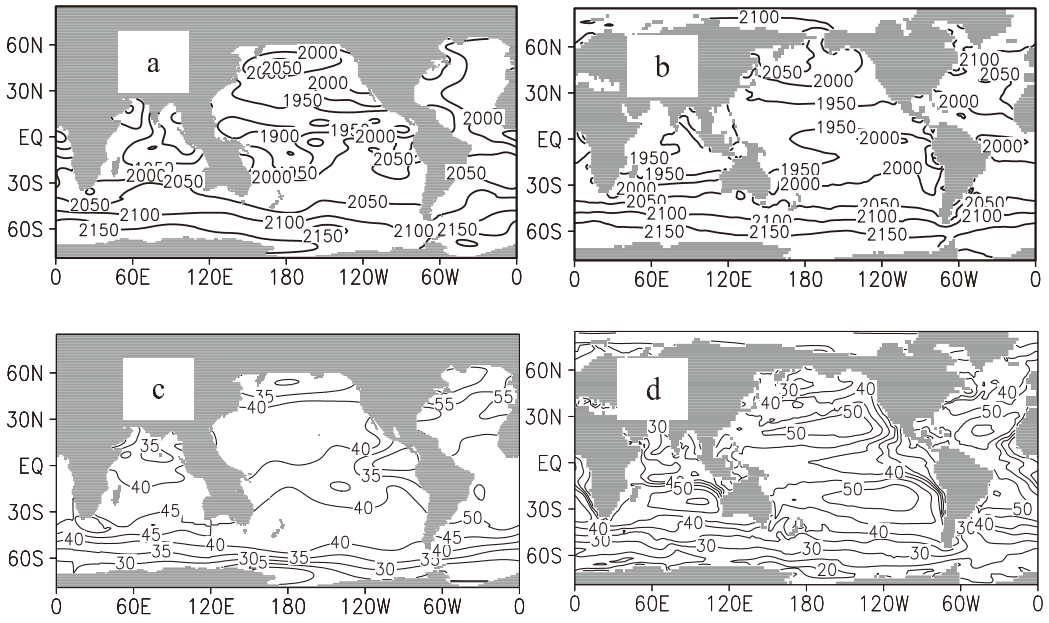

Fig. 9. Ten-year mean distributions of (a, b) DIC at sea surface and of (c, d) anthropogenic carbon at a depth of 75 m in the 1990s: (a, c) observations and (b, d) simulations. Contour intervals are 50 μmol kg^{-1} in (a, b) and 5 μmol kg^{-1} in (c, d), respectively.

observations, and can only be derived from the ocean tracer-based C* method (Gruber et al., 1996; Lee et al., 2003) based on other physical and biochemical data. Various surface water properties vary seasonally and interanuually. The data for anthropogenic carbon obtained from different time periods of cruise observations display an obvious difference in horizontal distribution characteristics between the surface and at a depth of 75 m, even showing opposite meridional gradients (data not shown). This phenomenon cannot be seen from other tracers. However, the model generates a small vertical difference of anthropogenic carbon in the mixed layer (data not shown). Because formation of the distribution characteristics of data-based surface anthropogenic carbon is not well understood, we do not discuss the difference in surface excess carbon between the simulation and the data-based estimate.

It can be seen from the 75-m depth results that the simulated results are basically in agreement with the data-based estimates. Because of the impact of vertical water movement, anthropogenic carbon concentrations are low in the equatorial upwelling region and the Southern Ocean, whereas in the subtropical regions the upper layer has high anthropogenic carbon concentrations because of slow vertical movement there. In addition, the absorbed anthropogenic carbon in the lower and higher latitude regions is transported into the subtropical regions through the wind-driven circulation, leading to the increase in anthropogenic carbon. The model overestimates the high anthropogenic carbon concentration observed in the subtropical regions. As pointed out by Li and Xu (2012), this is due to insufficient penetration and high surface accumulation (not shown).

The increase in surface DIC concentration from its pre-industrial state arises from the increase in the flux of absorbing atmospheric CO_2. Figures. 10a and b show the average air–sea ΔP_{CO_2} and CO_2 exchange flux for the 1990s, respectively. Compared with the pre-industrial distributions, the most obvious difference in ΔP_{CO_2} is that the -40 μatm contour in the eastern equatorial Pacific disappears, whereas in the subtropical region of the Pacific the area with positive ΔP_{CO_2} is clearly extended. For the CO_2 flux, the most obvious difference is that the positive area (outgassing area) significantly shrinks, particularly in the region south of 45°S where the main outgassing area has changed to a partial outgassing area or partial absorption area. The absorption strength in the other original absorption regions has been enhanced. This is in good agreement with climatological mean annual sea–air CO_2 flux for the reference year 2000 obtained with the ΔP_{CO_2} method by Takahashi et al. (2009). The eastern equatorial Pacific is the largest source, whereas the subtropical regions of both hemispheres and whole region north of 30°N in the Atlantic are sinks. Compared with the data-based results, our model underestimates the sink in the high-latitude region of the North Atlantic, and the source in the equatorial Pacific. This is caused by the simulated high and

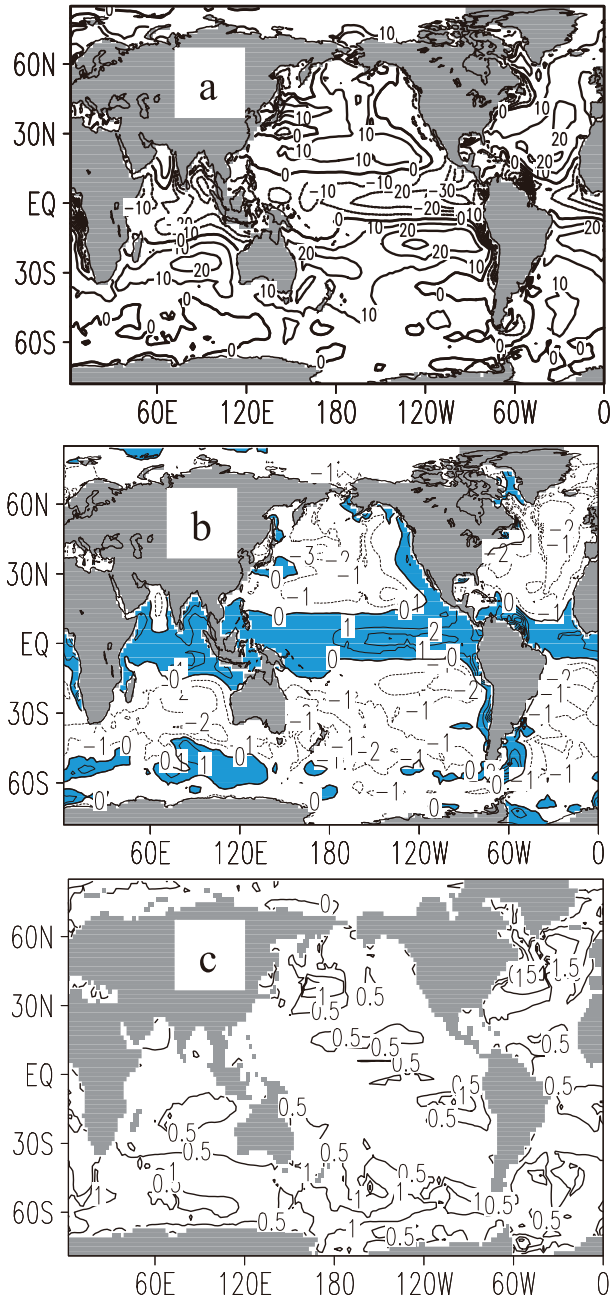

Fig. 10. Ten-year mean (a) air–sea P_{CO_2} difference ($P_{CO_{2a}} - P_{CO_{2o}}$, μatm) and (b) CO_2 fluxes (mol m^{-2} yr^{-1}) of total DIC, and (c) air–sea anthropogenic CO_2 fluxes in the 1990s. Contour intervals are 10, 1 and 0.5 in (a), (b) and (c), respectively.

low surface DIC concentrations there. In addition, simulation shows a weak sink in the subpolar region of the North Pacific, which is in contrast with the result reported by Takahashi et al. (2009). It is obtained from the accumulative calculation of Fig. 10b that in the 1990s the equatorial region (within ±15° of the equator) had an efflux of 0.59 Pg C yr^{-1} to the atmosphere, and both the northern (north of 15°N) and southern (south of 15°S) regions had an influx of 1.07 and 1.52 Pg C yr^{-1}, which is again smaller than that in 1990 estimated by Murnane et al. (1999). Furthermore, our release in the equatorial region is 18% smaller than that in 1990 estimated by Takahashi et al. (1997), but our uptake in both northern and southern regions is larger than that by Takahashi et al. (1997), particularly in the southern region where our value is 58% larger than that reported by Takahashi et al. (1997).

The subtraction of the pre-industrial air–sea CO_2 flux of natural carbon from the 1990s air–sea CO_2 flux (Fig. 10b) gives rise to the 1990s flux of anthropogenic carbon (Fig. 10c). Different from natural carbon, the anthropogenic carbon concentration decreases with increasing depth. Thus, for the air–sea flux, the regions with strong convection mixing and upwelling are a source of natural carbon but a sink for anthropogenic carbon. As shown in Fig. 10c, the Northwest Atlantic, the eastern equatorial Pacific, the Southern Ocean, and the Northwest Pacific are main absorption areas of anthropogenic carbon. Because of impacts of relatively high total alkalinity in the subtropical regions, these act as weak sinks of anthropogenic carbon (Li and Xu, 2012). Orr et al. (2001) compared the 1990 air–sea anthropogenic carbon flux obtained from the four OCMIP-1 models. The main absorption areas of anthropogenic carbon from the four models were consistent with our results. However, since the anthropogenic carbon flux is largely affected by the vertical movement, the difference in distributions of anthropogenic carbon flux from these four models is obvious because of their different physical fields. Our model results are relatively close to the results from the Princeton/GFDL model.

3.3 *Storage of anthropogenic carbon and the meridional transport of natural and anthropogenic carbon*

Figure 11 shows the data-based and model-based estimates of distributions of water column inventory of anthropogenic carbon as of 1994, and the difference between the simulated accumulative air–sea flux from 1800 to 1994 and inventory. The accumulative flux indicates the temporal integration of the flux from 1800 to 1994. The anthropogenic carbon data for the estimate are still from the GLODAP (Key et al., 2004). The region of NADP formation has the largest inventory, followed by the subtropical regions of both hemispheres, whereas the tropical region and the region near the Antarctic contain relatively small amounts of anthropogenic carbon because of the impact of shallow isopycnal surfaces. The source of data used here is the

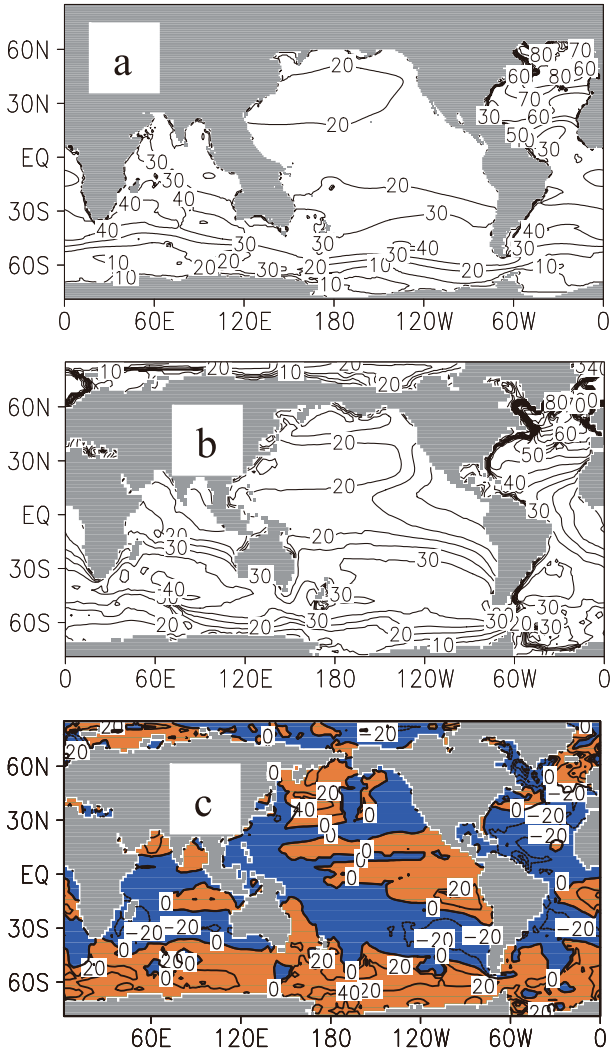

Fig. 11. Distributions of water column anthropogenic carbon inventory from (a) data-based and (b) model-based results, and of (c) the difference between accumulative anthropogenic carbon flux and anthropogenic carbon inventory in 1994.

same as in Sabine et al. (2004). Because of differences in data processing, it is noted that there are some differences in some regions between our Fig. 11 and Fig. 1 in Sabine et al. (2004). The most significant difference is that they have the center of lower than 10 mol m^{-2} in the western tropical Pacific. We consider that this low center is related to the data that have negative values below the 500-m depth. Nevertheless, the data with negative values are removed from our calculation of inventory. Our simulations are generally consistent with their data-based estimates in the whole distribution characteristics. A main difference is that model-based estimates are smaller in some regions, including in the North Atlantic and tropical Pacific. The small inventory in the North Atlantic is related to weak NADP that results in a shallow penetration of anthropogenic carbon, whereas in the tropical Pacific, particularly in the eastern equatorial Pacific, the small inventory is associated with the steep isopycnals in our model. These issues are related to our simulations that are based on the physical fields obtained from the forcing of climatological seasonally varying data. Use of interannully varying data as the forcing can effectively modify the insufficient penetration of anthropogenic carbon in the North Atlantic (Li et al., 2012).

Our model estimates 105 Pg C of anthropogenic carbon in the global ocean as of 1994, which is in the lower bound of other estimates (Sabine et al., 2004; Waugh et al., 2006; Khatiwala et al., 2009). Compared with the results by the perturbation approach in the same OGCM, our current estimate is larger than the estimate of 99 Pg C from the model forced by the climatologial seasonally varying data from the National Centers for Environmental Prediction (NCEP) reanalysis, but slightly smaller than the estimate of 107 Pg C from the model forced by the interannully varying data (Li et al., 2012). Using the same perturbation approach, the two cases from the last generation of OGCM (L30T63) give a global inventory of 87 and 93 Pg C in 1994 (Xu and Li, 2009). These comparisons demonstrate that improvement of simulations can be conducted from the different aspects, including use of more realistic forcing and modification of the OGCM.

Figure 11c (accumulative flux minus inventory) indicates that the region with large air–sea anthropogenic carbon flux (Fig. 10c) is the positive region where accumulative fluxes are larger than inventories, and correspondingly the other regions are negative. The large positive values in the high latitude regions of both the North Pacific and the Southern Ocean demonstrate that anthropogenic carbon is transported to other regions after it is absorbed from the atmosphere in these regions. The subpolar region of the North Atlantic is a sink of anthropogenic carbon from the atmosphere and also a storage region, so that the transported amount is small. The largest acceptance of anthropogenic carbon is located in the subtropical convergence regions where the locally absorbed anthropogenic carbon is not transported to other regions due to slow water movement there, and conversely the anthropogenic carbon in the other regions is transported there by advection and isopycnal diffusion. For example, large influx regions in the South Pacific are regions with steep isopycnal surfaces.

This interior migration characteristic is consistent with that of meridional transport (positive northward) reflected in Fig. 12. When meridional diffusion is ig-

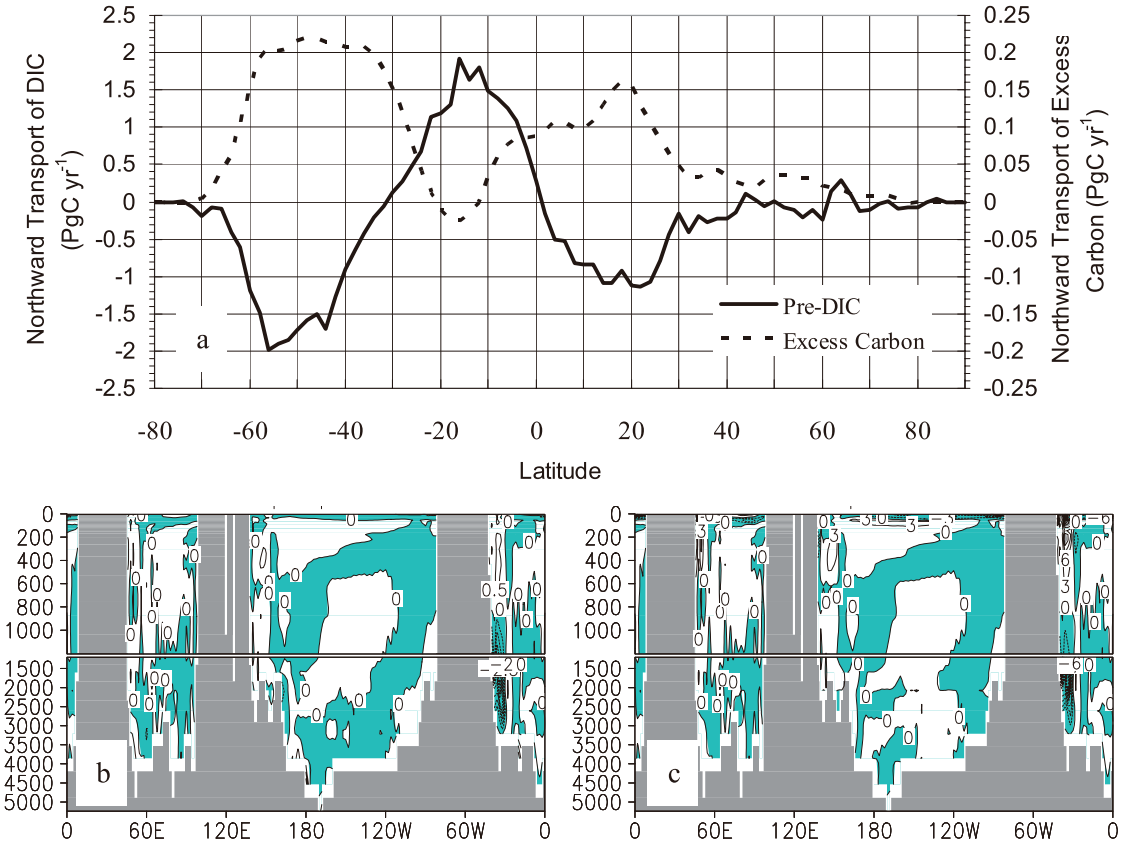

Fig. 12. (a) Northward transports of pre-industrial and anthropogenic DIC (Pg C yr^{-1}), and longitude–depth sections of meridional transport fluxes of (b) pre-industrial (10^6 mol s^{-1}) and (c) anthropogenic (10^3 mol s^{-1}) DIC at the equator in 2000. Contour intervals in (b) and (c) are 0.5.

nored, meridional transport (Eulerian velocity plus eddy-induced transport velocity) rate should be equal to the derivative of the difference between zonally integrated water column inventory and accumulative flux with respect to time. Thus, the maximum region of the difference should be near the zero region of transport rate. As shown in Fig. 12, the extremum of the transport rate of anthropogenic carbon appears to be at 48°S, 18°S and 18°N, with the value being 0.22 (largest, positive northward), −0.025 and 0.16 Pg C yr^{-1}, respectively. These latitudes in the Southern Hemisphere correspond to the zero regions in Fig. 11c, whereas in the Northern Hemisphere this type of correspondence exhibits a deviation. This is probably due to the difference between the North Pacific and North Atlantic being quite significant.

Since about 50% of anthropogenic carbon is stored at depths above 400 m (Sabine et al., 2004), the wind-driven circulation has more important effects on the advection transport of anthropogenic carbon. Figure 12a shows that the meridional transport direction of anthropogenic carbon is northward in most latitudes in 2000. The transport across the equator is 0.087 Pg C yr^{-1}, and the main southward transport appears to be at 12°– 20°S owing to the southward Ekman transport in the upper ocean layer that is an important part of the wind-driven circulation. In the Northern Hemisphere, the Ekman transport in the tropical and subtropical ocean is northward. In the regions north of 20°N, the wind-driven circulation also generates some northward meridional advection transport in the western boundary because the westward intensification exists in the real global ocean (Stommel, 1948), whereas in the eastern boundary the advection transport is the reverse, which can offset the western boundary transport to some extent. In the Northern Hemisphere, the southward transport from the mid-latitude subduction region in the Pacific Ocean is not strong enough because of the shallow penetration depth of anthropogenic carbon. Therefore, the meridional transport of anthropogenic carbon in the whole Northern Hemisphere is northward, especially in the northern tropical ocean. In the Southern Hemisphere, there is a strong uptake and subduction

along about 60°S, which induces a northward transport to the equator in the interior ocean. Furthermore, because the zonally integrated inventory of anthropogenic carbon is larger in the Southern Hemisphere than in the Northern Hemisphere, globally the strongest northward transport appears to be at the latitude bands of 30°–60°S in the Southern Hemisphere.

The transport characteristic of natural carbon is basically the opposite of anthropogenic carbon (Fig. 12a) because of different vertical distributions. In addition, the meridional transport of natural carbon can be derived from its air–sea fluxes. As known from Fig. 8, for natural carbon the region south of 50°S and the tropical region are main release areas of carbon, whereas the subtropical region is a main uptake area. Under the condition of an unchanged situation in column inventory of natural carbon, its interior meridional transport must be conducted from the subtropical region to high and low latitudes. Figure 12a displays the shift band of the south–north transport to be near 30°S in the Southern Hemisphere. This means that south of 30°S, natural carbon is transported toward high latitudes, whereas north of 30°S natural carbon is transported toward low latitudes. Near the equator, although meridional transport is close to zero, it receives the carbon from both northward and southward transports, so that it keeps a high release of natural carbon to the atmosphere.

Our simulation results are relatively consistent with those obtained by Murnane et al. (1999). The main difference is that south of 30°S the strength of southward transport is larger than that by Murnane et al. (1999). Sarmiento et al. (2000) compared the results of meridional transport of natural carbon from the three OGCMs. These three models all revealed northward transport in the Southern Hemisphere, in which the MPI model showed a relatively strong northward transport south of 30°S, and only the Princeton model generated a similar transport characteristic to our result, but south of 40°S the northward transport was close to 0, not negative. In these three models, only the Princeton model simulated a weak release of natural carbon to the atmosphere in the Southern Ocean, whereas the other two models gave a sink of natural carbon that is inconsistent with the result by Gruber et al. (2009) using the inversion method.

Nevertheless, there are some differences in natural carbon transport across the equator between our simulation and other simulations. Our simulation shows that a northward transport of natural DIC is 0.27 Pg C yr^{-1}, whereas other forward models (Sarmiento et al., 2000) and the results from the 3D model of atmospheric CO_2 transport (Keeling et al., 1989) showed that a cross-equatorial transport of natural DIC was southward or weakly northward. However, there is a large difference among their estimates. In the comparison of the three models by Sarmiento et al. (2000), the transport of DIC across the equator without river inputs ranged from 0.04 to −0.12 Pg C yr^{-1}, whereas the result reported by Keeling et al. (1989) was ∼ –1 Pg C yr^{-1} that was postulated to occur in the Atlantic Ocean.

Figures 12b and c show the vertical distributions of annual mean meridional transport fluxes of natural and anthropogenic DIC at the equator in 2000. Because of large differences in velocity between the surface and deep waters, to represent the large transport in the deep water due to thick layers, the results are treated to be the total flux of each vertical grid in units of mol s^{-1}. It is obvious that at the equator the main southward transport of natural carbon appears to be at a depth of 1000 to 3500 m where NADP is responsible for the transport. In the water above 1200 m, most regions have a northward transport. After basinal accumulation, a cross-equatorial northward transport of natural DIC is 0.93 and 0.42 Pg C yr^{-1} in the Pacific and Indian Oceans, respectively, whereas in the Atlantic Ocean this transport is southward, with the value being −1.08 Pg C yr^{-1}. Our estimate in the Atlantic Ocean is close to that reported by Keeling et al. (1989) but is higher than that from other forward models (Sarmiento et al., 2000) and from the inversion method by Mikaloff Fletcher et al. (2007). Our estimate in the Indo-Pacific Ocean is directionally consistent with that from the forward models (Sarmiento et al., 2000), but in the Pacific Ocean our estimate is different from the estimate of the southward transport by Mikaloff Fletcher et al. (2007). Furthermore, the magnitude of our estimate is much larger than their estimates. This leads to the fact that, globally, our model generates a northward transport of natural DIC.

In addition to DIC, the meridional transport of LDOC is also an important form of carbon transport in our model. Like anthropogenic DIC, vertical distribution characteristic of LDOC displays a decrease with depth. Therefore, the cross-equatorial transport in the Pacific, Indian and Atlantic Oceans is −0.14 Pg C yr^{-1}, −0.18 Pg C yr^{-1} and 0.16 Pg C yr^{-1}, respectively. Globally the meridonal transport of LDOC is −0.16 Pg C yr^{-1}. Thus, interhemispheric transport of pre-industrial total carbon (DIC+LDOC) is a northward transport of 0.11 Pg C yr^{-1}, exactly the same as the total release of 0.11 Pg C yr^{-1} in the Northern Hemisphere.

The meridional advection transport of anthropogenic DIC mainly occurs in the ocean above 600 m and at depths of 1 000–3 500 m in the North Atlantic (Fig. 12c). Except in the Atlantic Ocean, the pene-

tration of anthropogenic carbon in the other basins is relatively shallow (Xu and Li, 2009); anthropogenic carbon mainly appears to be in waters above 1500 m (Sabine et al., 2004). Hence, because of the impact of circulation in the upper ocean, the strongest meridional advection transport occurs at depths of above 600 m. The difference is that in the Pacific Ocean, the surface has a strong southward transport due to the Ekman transport, but the subsurface has a northward transport, whereas in both the Atlantic and Indian Oceans, the situation is the reverse. This is related to the slight difference in the pattern of the equatorial currents between the basins. The same situation is that there are northward transports at depths of 200–600 m. The basinal accumulation gives rise to cross-equatorial transport being -4.35×10^{-3} and -2.66×10^{-2} Pg C yr^{-1} in the Pacific and Indian Oceans, respectively. The southward transport of anthropogenic DIC in the deep waters of the North Atlantic is similarly caused by the southward transport of NADP. However, the meridional transport of anthropogenic DIC in the deep waters is not stronger than that in the upper ocean. As a result, the cross-equatorial transport in the whole Atlantic Ocean is northward, with the value being 0.12 Pg C yr^{-1}. This basinal difference in carbon transport is close to the result by Mikaloff Fletcher et al. (2006). According to their inversion results, in the Atlantic Ocean a northward cross-equatorial transport of anthropogenic DIC was 0.17 Pg C yr^{-1} in 1995, whereas in both the Indian and Pacific oceans, it was southward, with the value in the Indian Ocean being smaller than that in the Pacific Ocean, which includes the transport by Indonesian Throughflow. Under the impact of the Atlantic Ocean, globally accumulative cross-equatorial transport of anthropogenic DIC is northward, as shown in Fig. 12a.

4. Conclusions

An ocean biogeochemistry model (OBM) has been developed, which includes five prognostic variables of DIC, TA, phosphate, LDOC and DO. This OBM has been incorporated into a global ocean general circulation model (LICOM) to form an ocean biogeochemistry general circulation model (OBGCM). This OBGCM has been successfully used to study the cycling of both natural and anthropogenic carbon.

The steady state pre-industrial distributions of various prognostic variables generally show the observed characteristics. Simulated highest phosphate of over 1.8 μmol kg^{-1} is located south of 60°S, and the distribution in both the Northwest Atlantic and the equatorial region is also well simulated. A main deficiency of the model results is that the model underestimates phosphate concentrations by over 50% in the region north of 40°N in the North Pacific. Large export production is located in the regions of 30°– 60°N and 30°– 60°S as well as the eastern equatorial Pacific. The model estimates annual export production to be 12.5 Pg C yr^{-1}, which is in good agreement with that by different researchers using different approaches including the observation-based and model-based estimates. Apart from TA in the subtropical region of the North Atlantic being underestimated by our model, the surface distribution characteristics of TA and DIC are consistent with observed ones. The steady state pre-industrial air–sea CO_2 flux clearly shows the carbon loss to the atmosphere in both the tropical region and Southern Ocean, and the carbon gain from the atmosphere in the subtropical regions, which is strongly consistent with that obtained by other researchers using the inversion method. The model reveals that the global region within ±15° of the equator in pre-industrial times had an efflux of 0.97 Pg C yr^{-1} that was offset by the gain of CO_2 in the other regions.

The surface DIC distribution of the 1990s clearly indicates the increase of 20–50 μmol kg^{-1} in carbon concentration. The simulated results are highly consistent with the observations except that the model value is over 20 μmol kg^{-1} larger than the observed one in the region north of 55°N in the North Atlantic. The difference in DIC concentrations between the post-industrial and pre-industrial ages gives rise to excess carbon (i.e. anthropogenic carbon). Simulated results from a depth of 75 m in the 1990s are basically in agreement with the data-based estimates, including low concentrations in the equatorial upwelling region and the Southern Ocean, and high concentrations in the subtropical regions. Compared with the pre-industrial air–sea CO_2 flux, the area of release of CO_2 to the atmosphere is reduced but the absorption strength is obviously enhanced in the 1990s. The simulated results are in agreement with those reported by Takahashi et al. (2009) using the ΔP_{CO_2} method. Unlike natural carbon, the regions where there are sources of natural carbon are probably important sinks for anthropogenic carbon, such as the tropical region and the Southern Ocean and the Northwest Pacific.

The distribution characteristic of the model-based estimates of anthropogenic carbon inventory is consistent with that of the data-based estimates. Our model estimates that the global ocean contained 105 Pg C of anthropogenic carbon as of 1994, which is in the lower bound of other observation-based estimates. It is clearly obtained that the Southern Ocean and the high-latitude region of the North Pacific are important export regions, whereas the subtropical re-

gions are the largest acceptance areas of anthropogenic carbon. The south– north transports of both natural and anthropogenic DIC are calculated from the simulation. Although our results about the meridional transport are relatively consistent with those by the Princetion model, there is a difference in the cross-equatorial transport. Our results of natural and anthropogenic DIC across the equator are globally 0.27 and 0.087 Pg C yr^{-1}. The results from most researches show a southward or weak northward transport of natural DIC, although there is a large difference among those estimates. However, our 1.08 Pg C yr^{-1} southward transport of natural DIC in the Atlantic Ocean is quite close to that by Keeling et al. (1989). Globally interhemispheric transport of total natural carbon, including natural DIC and LDOC, is 0.11 Pg C yr^{-1} (northward), which is exactly equal to the loss of carbon to the atmosphere in the Northern Hemisphere. Further analysis of the meridional transport fluxes across the equator shows that the strongest transport of natural carbon is carried by the southward transport of the deep waters in the North Atlantic. The meridional transport across the equator in both the Pacific and Indian Oceans represents the northward transport and offsets the southward transport due to NADP. The cross-equatorial transport of anthropogenic DIC is mainly affected by the upper circulation of above 600 m. The main contribution is from the Atlantic Ocean.

Acknowledgements. This work was supported by the National Basic Research Program of China ("973 program", Grant No. 2010CB951802) and the National Natural Science Foundation of China (Grant Nos. 40730106, 41105087, and 41075091).

REFERENCES

Anderson, L., and J. Sarmiento, 1995: Global ocean phosphate and oxygen simulations. *Global Biogeochemical Cycles*, **9**, 621–631.

Aumont, O., J. C. Orr, P. Monfray, G. Madec, and E. Maier-Reimer, 1999: Nutrient trapping in the equatorial Pacific: The ocean circulation solution. *Global Biogechemical Cycles*, **13**(2), 351–369.

Aumont, O., E. Maier-Reimer, S. Blain, and P. Monfray, 2003: An ecosystem model of the global ocean including Fe, Si, P colimitations. *Global Biogeochemical Cycles*, **17**(2), 1060, doi: 10.1029/2001GB001745.

Bacastow, R., and E. Maier-Reimer, 1990: Ocean-circulation model of the carbon cycle. *Climate Dyn.*, **4**, 95–125.

Craig, H., 1957: The natural distribution of radiocarbon and the exchange time of carbon dioxide between atmosphere and sea. *Tellus*, **9**, 1–17.

Doney, S. C., and Coauthors, 2004: Evaluating global ocean carbon models: The importance of realistic physics. *Global Biogeochemical Cycles*, **18**, GB3017, doi: 10.1029/2003GB002150.

Dong, T. L., M. X. Wang, and R. Z. Liu, 1994: Two-dimensional atmospheric CO_2-Atlantic carbon cycle model. *Chinese J. Atmos. Sci.*, **18**, 631–640. (in Chinese)

Enting, I. G., T. M. Wigley, and M. Heimann, 1994: Future emissions and concentration of carbon dioxide: Key ocean/atmosphere/land Analysis. CSIRO Division of Atmospheric Research Technical Paper, No. 31, CSIRO, Australia, 120pp.

Eppley, R. W., and B. J. Peterson, 1979: Particulate organic matter flux and planktonic new production in the deep ocean. *Nature*, **282**(13), 677–680.

Eppley, R. W., J. N. Rogers, and J. J. McCarthy, 1969: Half saturation constants for uptake of nitrate and ammonium by marine phytoplankton. *Limnology and Oceanography*, **14**, 912–920.

Esbensen, S. K., and Y. Kushnir, 1981: The heat budget of the global ocean: An atlas based on estimates from surface marine observations. Rep. 29, Climatic Research Institute, Oregon State University, Corvallis, 244pp.

Garcia, H. E., and L. I. Gordon, 1992: Oxygen solubility in seawater: Better fitting equations. *Limnology and Oceanography*, **37**, 1307–1312.

Garcia, H. E., R. A. Locarnini, T. P. Boyer, and J. I. Antonov, 2006a: *Disssolved Oxygen, Apparent Oxygen Utilization, and Oxygen Ssturation*. Vol. 3, *World Ocean Altas*, 2005, S. Levitus, Ed., *NOAA Atlas NESDIS 63*, U.S. Government Printing Office, Washington, D.C., 342pp.

Garcia, H. E., R. A. Locarnini, T. P. Boyer, and J. I. Antonov, 2006b: *Nutrients (phosphate, nitrate, and silicate)*. Vol. 4, *World Ocean Altas*, 2005, S. Levitus, Ed., *NOAA Atlas NESDIS 64*, U.S. Government Printing Office, Washington, D.C., 396pp.

Gent, P. R., and J. C. McWilliams, 1990: Isopycnal mixing in ocean circulation models. *J. Phys. Oceanogr.*, **20**, 150–155.

Gent, P. R., J. Willebrand, and T. J. McDougall, 1995: Parameterizing eddy-induced tracer transports in ocean circulation models. *J. Phys. Oceanogr.*, **25**, 463–474.

Gloor, M., N. Gruber, J. Sarmiento, C. L. Sabine, R. A. Feely, and C. Roedenbeck, 2003: A first estimate of present and pre-industrial air-sea CO_2 fluxes patterns based on ocean interior carbon measurements and models. *Geophys. Res. Lett.,* **30**(1), 1010, doi: 10.1029/2002GL015594.

Gruber, N., J. L. Sarmiento, and T. F. Stocker, 1996: An improved method for detecting anthropogenic CO_2 in the oceans. *Global Biogeochemical Cycles*, **10**(4), 809–837.

Gruber, N., and Coauthors, 2009: Oceanic sources, sinks, and transport of atmospheric CO_2. *Global Biogeochemical Cycles,* **23**, GB1005, doi: 1029/2008GB003349.

IPCC, 2001: *Climate Change 2001: The Scientific Basis. Contribution of Working Group I to the Third Assessment Report of the Intergovermental Panel on Climate Change*, J. T. Houghton et al., Eds. Cambridge University Press, Cambridge, UK and New York, USA, 881pp.

IPCC, 2007: *Climate change 2007: The Physical Science Basis. Contribution of Working Group I to the Third Assessment Report of the Intergovermental Panel on Climate Change*, S. Solomon et al., Eds., Cambridge University Press, Cambridge, United Kingdom and New York, USA, 996pp.

Jin, X., and G. Y., Shi, 1999: Numerical modeling for distribution of carbon and nutrient in the ocean. *Climatic and Environmental Research*, **4**(4), 375–387. (in Chinese)

Jin, X., and G. Y., Shi, 2001: The role of biological pump in ocean carbon cycle. *Chinese J. Atmos. Sci.*, **25**, 683–688. (in Chinese)

Keeling, C. D., S. C. Piper, and M. Heimann, 1989: A three-dimensional model of atmospheric CO_2 transport based on observed winds: 4 mean annual gradients and interannual variations. *Aspects of Climate Variability in the Pacific and the Western Americas*, D. H. Peterson, Ed., Geophys. Monogr. Ser., vol. 55, AGU, Washington D.C., 305–363.

Key, R. M., and Coauthors, 2004: A global ocean carbon climatology: Results from global data analysis project (GLODAP). *Global Biogeochemical Cycles*, **18**, GB4031, doi: 10.1029/2004GB002247.

Khatiwala, S., F. Primeau, and T. Hall, 2009: Reconstruction of the history of anthropogenic CO_2 concentrations in the ocean. *Nature*, **462**, 346–349.

Laws, E. A., P. G. Falkowski, W. O. Smith Jr., H. Ducklow, and J. J. McCarthy, 2000: Temperature effects on export production in the open ocean. *Global Biogeochemical Cycles*, **14**(4), 1231–1246.

Lee, K., and Coauthors, 2003: An updated anthropogenic CO_2 inventory in the Atlantic Ocean. *Global Biogeochemical Cycles*, **17**(4), 1116, doi: 10.1029/2003GB002067.

Levine, N. M., S. C. Doney, R. Wanninkhof, K. Lindsay, and I. Y. Fung, 2008: Impact of ocean carbon system variability on the detection of temporal increases in anthropogenic CO_2. *J. Geophys. Res.*, **113**, C03019, doi: 10.1029/2007JC004153.

Li, Q. Q., and G. Y. Shi, 2005: Simulation of ^{14}C in IAP/LASG L30T63 ocean model. *Acta Meteorologica Sinica*, **19**, 436–446.

Li, Y. C., and Y. F. Xu, 2012: Uptake and storage of anthropogenic CO_2 in the Pacific Ocean estimated using two modeling approaches. *Adv. Atmos. Sci.*, **29**(4), 795–809, doi: 10.1007/s00376-012-1170-4.

Li, Y. C., Y. F. Xu, L. Zhao, and M. X. Wang, 2006: Preliminary study of the simulated distribution of CFC-11 in the global ocean circulation model. *Chinese J. Atmos. Sci.*, **30**(4), 671–681. (in Chinese)

Li, Y. C., Y. F. Xu, L. Zhao, and M. X. Wang, 2007: Sensitivity of CFC-11 uptake in a global ocean model to subgrid-scale mixing parameterization. *Acta Oceanologica Sinica*, **29**(3), 31–38. (in Chinese)

Li, Y. C., Y. F. Xu, M. Chu, and Y. Q. Yu, 2012: Influences of climate change on the uptake and storage of anthropogenic CO_2 in the global ocean. *Acta Meteorologica Sinica*, **26**(3), 304–317, doi: 10.1007/s13351-012-0304-z.

Liu, H. L., X. H. Zhang, W. Li, Y. Y. Yu, and R. C. Yu, 2004: An eddy-permitting oceanic general circulation model and its preliminary evaluation. *Adv. Atmos. Sci.*, **21**, 675–690.

Maier-Reimer, E., 1993: Geochemical cycles in an ocean general circulation model: Preindustrial tracer distributions. *Global Biogeochemical Cycles*, **7**(3), 645–677.

Marinov, I., A. Gnanadesikan, J. L. Sarmiento, J. R. Toggweiler, M. Follows, and B. K. Mignone, 2008: Impact of oceanic circulation on biological carbon storage in the ocean and atmospheric pCO_2. *Global Biogeochemical Cycles*, **22**, GB30007, doi: 10.1029/2007GB002958.

Mikaloff Fletcher, S. E., and Coauthors, 2006: Inversion estimates of anthropogenic CO_2 uptake, transport, and storage by the ocean. *Global Biogeochemical Cycles*, **20**, GB2002, doi: 10.1029/2005GB002530.

Mikaloff Fletcher, S. E., and Coauthors, 2007: Inverse estimates of the oceanic sources and sinks of natural CO_2 and the implied oceanic carbon transport. *Global Biogeochemical Cycles*, **21**, GB1010, doi: 10.1029/2006GB002751.

Millero F. J., K. Lee, and M. Roche., 1998: Distribution of alkalinity in the surface waters of the major oceans. *Marine Chemistry*, **60**, 111–130.

Murnane, R. J., J. L. Sarmiento, and C. Le Quere, 1999: Spatial distribution of air-sea CO_2 fluxes and the interhemisopheric transport of carbon by the oceans. *Global Biogeochemical Cycles*, **13**, 287–305.

Najjar, R. G., J. L. Sarmiento, and J. R. Toggweiler, 1992: Downward transport and fate of organic matter in the ocean: Simulations with a general circulation model. *Global Biogeochemical Cycles*, **6**, 45–76.

Najjar, R. G., and Coauthors, 2007: Impact of circulation on export production, dissolved organic matter and dissolved oxygen in the ocean: Results from phase II of the ocean carbon-cycle model intercomparison project (OCMIP-2). *Global Biogeochemical Cycles*, **21**, GB3007, doi: 10.1029/2006GB002857.

Oeschger, H., U. Sigenthaler, U. Schotterer, and A. Gugelman, 1975: A box diffusion model to study the carbon dioxide exchange in nature. *Tellus*, **27**, 168–192.

Orr, J., and Coauthors, 2001: Estimates of anthropogenic carbon uptake from four 3-D global ocean models. *Global Biogeochemical Cycles*, **15**, 43–60.

Palmer, J. R., and I. J. Totterdell, 2001: Production and export in a global ocean ecosystem model. *Deep-Sea Res. I*, **48**, 1169–1198.

Pu, Y. F., and M. X. Wang, 2000: An ocean carbon cycle

model Part I: Establishing of carbon model including an oceanic dynamic general circulation field, chemical, physical and biological processes occurred in the ocean. *Climatic and Environmental Research*, **5**(2), 129–140. (in Chinese)

Roeske, F., 2001: An atlas of surface flues based on the ECMWF re-analysis-a climatological dataset to force global ocean general circulation models. Report No. 323, Max-Planck-Institut für Meteorologie, Hamburg, 1–31.

Sabine, C. L., and Coauthors, 2004: The oceanic sink for anthropogenic CO_2. *Science*, **305**(16), 367–371.

Sarmiento, J. L., J. C. Orr, and U. Siegenthaler, 1992: A perturbation simulation of CO_2 uptake in an ocean general circulation mode. *J. Geophys. Res.*, **97**, 3621–3645.

Sarmiento, J. L., P. Monfray, E. Maier-Reimer, O. Aumont, R. J. Murnane, and J. C. Orr, 2000: Sea-air CO_2 fluxes and carbon transport: A comparison of three ocean general circulation models. *Global Biogeochemical Cycles*, **14**(4), 1267–1281.

Schlitzer, R., 2002: Carbon export in the southern Ocean: Results from inverse modeling and comparison with satellite-based estimates. *Deep-Sea Res. II*, **49**, 1623–1644.

Schmittner, A., A. Oschlies, X. Giraud, M. Eby, and H. L. Simmons, 2005: A global model of the marine ecosystem for long term simulations: Sensitivity to ocean mixing, buoyancy forcing, particle sinking and dissolved organic matter cycling. *Global Biogeochemical Cycles*, **19**, GB3004, doi: 10.1029/2004GB002283.

Six, K. D., and E. Maier-Reimer, 1996: Effects of plankton dynamics on seasonal carbon fluxes in an ocean general circulation model. *Global Biogeochemical Cycles*, **10**(4), 559–583.

Stommel, 1948: The westward intensification of wind-driven ocean currents. *Trans. Amer. Geophys. Union*, **29**, 202–206.

Sweeney, C., E. Gloor, A. R. Jacobson, R. M. Key, G. Mckinley, J. L. Sarmietnto, and R. Wannikhof, 2007: Constraining global air-sea gas exchange for CO_2 with recent bomb ^{14}C measurements. *Global Biogeochemical Cycles*, **21**, GB2015, doi: 10.1029/2006GB002784.

Takahashi, T., R. A. Feely, R. Weiss, R. H. Wanninkhof, D. W. Chipman, S. C. Sutherland, and T. T. Takahashi, 1997: Global air-sea flux of CO_2: An estimate based on measurements of sea-air pCO_2 difference. *Proc. Natl. Acad. Sci.*, **94**, 8292–8299.

Takahashi, T., and Coauthors, 2009: Climatological mean and decadal change in surface ocean pCO_2, and net sea-air CO_2 flux over the global oceans. *Deep-Sea Res. II*, **56**, 554–577.

Wanninkhof, R., 1992: Relationship between wind speed and gas exchange over the ocean. *J. Geophys. Res.*, **97**, 7373–7382.

Waugh, D. W., T. M. Hall, B. I. McNeil, R. Key, and R. J. Matear, 2006: Anthropogenic CO_2 in the oceans estimated using transit time distributions. *Tellus* (*B*), **58**(5), 376–389.

Weiss, R. F., 1974: Carbon dioxide in water and seawater: The solubility of a nonideal gas. *Marine Chemistry*, **2**, 203–215.

Wu, J. F., W. Sunda, E. A., Boyle, and D. M. Karl, 2000: Phosphate depletion in the western North Atlantic Ocean. *Science*, **289**, 759–762.

Xing, R. N., 1995: Three-dimensional model of the carbon cycle in the ocean. *Journal of Beijing Meteorological College*, **2**, 37–41. (in Chinese)

Xing, R. N., 2000: A three-dimensional world ocean carbon cycle model with ocean biota. *Chinese J. Atmos. Sci.*, **24**, 333–340. (in Chinese)

Xu, Y. F., 1992: The buffer capability of the ocean to increasing CO_2. *Adv. Atmos. Sci.*, **9**, 501–510.

Xu, Y. F., and Y. C. Li, 2009: Estimates of anthropogenic CO_2 uptake in a global ocean model. *Adv. Atmos. Sci.*, **26**(2), 265–274, doi: 10.1007/s00376-009-0265-z.

Yamanaka, Y., and E. Tajika, 1996: The role of the vertical fluxes of particulate organic matter and calcite in the oceanic carbon cycle: Studies using an ocean biogeochemical general circulation model. *Global Biogeochemical Cycles*, **10**, 361–382.